AIAA

A01-16707

AIAA 2001-0892
Numerical Simulation of Receptivity and Stability of Nonequilibrium Reacting Hypersonic Boundary Layers

Yanbao Ma and Xiaolin Zhong
University of California, Los Angeles

39th Aerospace Sciences Meeting & Exhibit
January 8–11, 2001 / Reno, NV

Numerical Simulation of Receptivity and Stability of Nonequilibrium Reacting Hypersonic Boundary Layers

Yanbao Ma*and Xiaolin Zhong[†]

University of California, Los Angeles, CA 90095

1 Abstract

A high-order upwind finite difference shock fitting scheme and semi-implicit method is applied in the simulation of transient nonequilibrium hypersonic boundary-layer flows. The results from TVD method are used as inflow conditions to commence numerical simulation of hypersonic flow over flat plates by shock-fitting method, which are validated by comparing the numerical results with experimental resutls. The receptivities to three different types of forcing disturbances for a Mach 4.5 flow over a flat plate are studied. A LST-code based on multi-domain spectral method is also developed to identify instability modes. The results of stability from DNS are compared with that of LST prediction. The receptivity coefficient for flow over a flat plat at $Mach4.5$ to plane acoustic waves at zone angle is close to 1. The receptivity and stability of a Mach 10 oxygen flow over a flat plate is studied in both perfect gas and thermochemically nonequilibrium regime. Real gas effect is destabilizing for the boundary-layer disturbances in this case.

2 Introduction

The design of future space transportation vehicles, especially the development of new cheaper reusable launch systems, cause great interest to investigate hypersonic nonequilibrium flow. The laminar-turbulent transition of hypersonic boundary layer significantly affects the vehicle performance and surface heating. Therefore, the accurate prediction of boundary layer transition is a critical part for aerodynamic design of vehicle and thermal protection system. In an environment with small initial disturbances, which is true in most flight conditions of hypersonic vehicles, the paths to transition can conceptually be divided into

---

*Graduate Student Researcher, Department of Mechanical and Aerospace Engineering

[†]Associate Professor, Department of Mechanical and Aerospace Engineering, Associate Fellow AIAA.

three stages: 1) receptivity, 2) linear eigenmode growth or transient growth, and 3) nonlinear breakdown to turbulence. The first stage, receptivity process, converts the environmental disturbances into instability, Tollmien-Schlichting (T-S), waves in the boundary layers. The second stage is the linear eigenmode growth of boundary-layer instability waves obtained as the eigensolutions of the homogeneous linearized disturbance equations. As the amplitude grows, three-dimensional and nonlinear interactions occur in the form of secondary instabilities [1]. Subsequent stages is the breakdown to turbulence. This process is strongly influenced by and dependent on freestream and wall conditions. The receptivity to large-amplitude disturbance may lead to transition without the appearance of the second stage, which is called bypass transition. In real flight conditions, external disturbances common to the flight environment are typically small. Therefore, three-stage transition process is more important than bypass transition for practical space transportation vehicles.

The most widely used transition prediction method is e^N method, which was developed by Smith and Gamberoni [2] and Van Ingen [3]. This method postulates that boundary layer transition occurs when the total growth of the most unstable disturbance exceeds some empirical factor, N, relative to its amplitude at the lower branch (Branch I) of neutral stability point. The disturbance growth is calculated from linear stability theory (LST). Typical value of N determined by comparison with experimental observation of transition location is between 9 and 11. This criteria is limited because only the linear growth of disturbance is considered and it is independent of the freestream disturbance environment and geometry of model. Measurements of the transition on a pointed cone by Krogmann [4] in the Ludwieg tube showed higher transition Reynolds numbers than those measured in other facilities under the same flow conditions. Beckwith [5] found that the transition location might be independent on the unit Reynolds number (Re_∞) in his experiment. In contract, the measurements in other facilities by Pate [6,7] Potter [8,9] and in free-flight conditions showed the transition Reynolds number increased with increasing unit Reynolds number. Even in the same wind tunnel, Stainback et al [10] found the correlation of transitional

Reynolds number (R_{e_T}) is proportional to $Re_\infty^{0.45}$, while Softly et al [11] found that the Re_∞ dependence disappears for some operating conditions. Stetson et al [12] studied the unit Reynolds number and environmental effects on the transition of a cone at Mach 8 and drew a conclusion that knowledge of the stability characteristics of a boundary layer was only part of the problem and the external disturbances must be prescribed in order to make a boundary layer transition prediction based upon stability considerations. These measurements and others shows that transition point (R_{e_T}) is strongly affected by the specific details of the free-stream disturbance environment. Therefore, while the value of N is calibrated for a particular tunnel and model, there is no reason to expect that value of N to be consistent with measurements of same model in other different tunnel or measurements of different models in the same tunnel. Needless to say, it is difficult to give an accurate estimate of transition location of vehicle in the real flight condition by extending the results obtained from wind tunnel experiments based on e^N method. Transition to turbulence will never be successfully understood or predicted without answering how environmental disturbances enter the boundary layer and ultimately generate unstable waves. The process how environment disturbance enters boundary layer and triggers instability waves is termed the receptivity phenomenon. The receptivity mechanism provides important initial conditions of amplitude, frequency, and phase for the instability waves in the boundary layers [13-15]. The goal of receptivity analysis is to improve current transition prediction method by including characteristic of freestream disturbance environment and geometry information.

When an aerospace vehicle travels through the atmosphere at hypersonic speed, the bow shock which envelopes the vehicle is pushed so close to the edge of boundary layer that the effect of shock must be considered in the study of transition of hypersonic boundary layer. In addition, the shock converts the kinetic energy of the stream to internal energy, raising the temperature to a value where real gas effects due to excitation of vibrational energy and chemical reaction are required to be considered.

To date, there has been considerable theoretical, numerical and experimental research on the receptivity, instability, and transition of hypersonic boundary layer flows. However, many questions remain regarding the complex transition mechanisms involved in nonequilibrium hypersonic boundary layer flow.

The main purpose of this paper is to study the receptivity and stability of hypersonic boundary layer to freestream disturbances by using numerical simulation.

To study the real gas effects on the receptivity and stability of hypersonic boundary-layer flow, reacting O_2 flow over a flat plate is studied in both perfect gas and thermochemically nonequilibrium regime. In order to support our main efforts in the direct numerical simulation, a LST code based on multi-domain spectral method is also developed. The results of LST can be used to find the frequency of most unstable mode for fixed Reyndolds number and Mach number. It can also be useful to identify different modes and decompose different modes from DNS results.

3 Governing Equations and Physical Model

3.1 Governing Equations

The governing equations are formulated for a two-temperature model with two species (non-ionizing) finite rate chemistry under the assumption that the rate of rotational relaxation approachs infinity, and the rotational energy is fully excited (i.e., rotational temperature equals translational temperature). In conservative form, the Navier-Stokes equations, along with vibrational energy equations, are:

$$\frac{\partial \mathbf{U}}{\partial t} + \frac{\partial}{\partial x}(\mathbf{F}_1 + \mathbf{F}_{v1}) + \frac{\partial}{\partial y}(\mathbf{F}_2 + \mathbf{F}_{v2})$$
$$+ \frac{\partial}{\partial z}(\mathbf{F}_3 + \mathbf{F}_{v3}) = \mathbf{W} \qquad (1)$$

$$U = \{\rho_1, \ \rho_2, \ \rho u_1, \ \rho u_2, \ \rho u_3, \ E_v, \ E\}^T \qquad (2)$$

$$\mathbf{W} = \{w_1, \ -w_1, \ 0, \ 0, \ 0, \ w_v \ 0\}^T \qquad (3)$$

where E_v and E are the vibrational and total energies per unit volume, the w_1 is the chemical source terms, and w_v is the source terms for the vibrational mode. $F_{j=1,2,3}$ are the inviscid fluxes, and $F_{vj=1,2,3}$ are the viscous fluxes. Reacting O_2 flows are considered in this study.

3.2 State Equations and Source Terms

The system is taken to be a mixture of thermally perfect gases with the following equation of state:

$$p = \rho R T_t, \qquad \rho = \rho_1 + \rho_2 \qquad (4)$$

where p and ρ are the bulk pressure and density, respectively, T_t is the translational temperature. The vi-

2

brational and total energies per unit volume are given by:

$$E_v = \sum_{i=1}^{nd} \rho_i e_{vi}, \qquad E = \sum_{i=1}^{NS} \rho_i e_i + \rho \frac{u^2 + v^2}{2} \qquad (5)$$

The reaction model is given as:

$$O_2 + M_i \;\; \rightleftharpoons \;\; O + O + M_i \qquad (6)$$
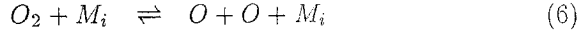
where M_i denotes any of the i species. Reaction rates are following Park' chemistry model [16,17]. The components of total energy and transport coefficients are described in detail in our previous work [18].

4 Numerical Methods and Boundary Conditions

4.1 Numerical Methods

Fifth-order upwind finite difference schemes are applied for convective terms while sixth-order central schemes for the discretization of viscous terms [19].

The spatial discretization of the governing equations leads to a system of first-order ordinary differential equations. Third-order Semi-implicit Runge-Kutta schemes [20] are used for temporal discretization. The governing equations are additively split into stiff and non-stiff terms in the form of

$$\frac{d\mathbf{U}}{dt} = \mathbf{F}(\mathbf{U}) + \mathbf{G}(\mathbf{U}) \qquad (7)$$

where $\mathbf{U}$ is the vector of discretized flow field variables, $\mathbf{F}$ is non-stiff terms resulted from spatial discretization of the flux terms which can be computed explicitly, and $\mathbf{G}$ is stiff thermo-chemical source terms which need to be computed implicitly.

For numerical simulation with source term, it is necessary to exactly evaluate the Jacobian of source vector $\mathbf{C} = \partial \mathbf{W}/\partial \mathbf{U}$. $\mathbf{W}$ can be expressed as a function of the temperature

$$\mathbf{W}(\mathbf{U}) = \tilde{\mathbf{W}}(\mathbf{U}, T(\mathbf{U}), T_v(\mathbf{U})), \qquad (8)$$

and Jacobian can be written as

$$\mathbf{C} = \frac{\partial \tilde{\mathbf{W}}}{\partial \mathbf{U}} + \frac{\partial \tilde{\mathbf{W}}}{\partial T}\frac{\partial T}{\partial \mathbf{U}} + \frac{\partial \tilde{\mathbf{W}}}{\partial T_v}\frac{\partial T_v}{\partial \mathbf{U}} \qquad (9)$$

The derivation of Jacobian can be found in [21]

4.2 Boundary Conditions

No-slip condition for velocity adiabatic wall condition for temperature are used. In this study, the wall is assumed to be noncatalytic. The Rankine-Hugoniot relations across the shock are used at shock boundary. The results from TVD are used as inflow conditions, which is discussed in more detail in latter section. High order extrapolation is used for outflow conditions because the flow is hypersonic at the outlet except that there is a tiny region near the wall where flow is subsonic.

5 Code Validation

In the simulation, the results near the leading edge from the second-order TVD shock capturing method are used as inflow conditions to commence DNS by shock-fitting method. The validation of TVD results are examined by comparing the numerical results with experimental results. Before the study of receptivity of hypersonic nonequilibrium flow, a Mach 4.5 flow over a flat plate is investigated in perfect gas regime as a test case.

5.1 Validation of Inflow Conditions from TVD Results

5.1.1 Steady hypersonic perfect gas flow at $M_\infty = 5.79$

The flow conditions are following Kendall's [22] experiment:

$$M_\infty = 5.79 \qquad\qquad T_\infty = 49.368\,K$$
$$p_\infty = 253.4886\,Pa \qquad Pr = 0.72$$
$$Re_\infty = \rho_\infty U_\infty/\mu_\infty = 4.61 \times 10^6/m$$

Besides of TVD method, we also use another code to calculate the mean flow, which is developed by Zhong and Lee [23] based on WENO shock capturing method. After obtaining the convergence steady flow, we use the

3

profiles located at $X = 0.18inch$ as the inflow conditions to start our shock-fitting calculation. 200×200 grids are used for TVD method and 160×100 grids are used for shock-fitting method. Here, we choose the convergent results from TVD other than WENO as inflow conditions for shock-fitting method because TVD solution is more stable all though it is more dissipative. The shock position at the inflow is given by the location of maximum pressure is shown in Fig. 1 and compared with experimental results. Overall, numerical results match experiment very well. Fig. 2 shows the velocity profiles at $X = 0.64inch$. There is good agreement between numerical and experimental results except that there is visible difference close to wall surface. This is because the velocity very close to the wall is difficult to measure in experiment.

5.2 Receptivity and Stability of Flow over a Flat Plate at $M_\infty = 4.5$

The flow conditions are following Kendall's [24] experiment:

$$M_\infty = 4.5 \qquad T_\infty = 65.15\,K$$
$$p_\infty = 728.4381557 Pa \qquad Pr = 0.72$$
$$Re_\infty = \rho_\infty U_\infty / \mu_\infty = 7.2 \times 10^6 / m$$

We distribute very fine grids (200×200) near the leading edge in TVD method to get accurate inflow conditions for shock-fitting calculation. The pressure contours from TVD method and fifth-order shock-fitting method are shown in Fig. 3. Overall, there is excellent agreement, although there exists visible difference in the downstream between the contours from two different methods, which is due to the low order accuracy and high dissipation of TVD method. The profiles of normal velocity at $X = 0.007m$ is shown in Fig. 4. Despite the dissipation of TVD method near the shock, the agreement is excellent. Therefore, we can use the TVD solution as inflow condition to start our high-order calculation by shock-fitting method.

The computational domain by using shock fitting method begins at $x = 0.006m$ and ends at $0.307m$, corresponding to the local Reynolds numbers ranging from $Re_x = 0.432 \times 10^5$ to $Re_x = 2.21 \times 10^6$. In the studies of boundary stability, the Reynolds number based on the length scale of boundary layer thickness, are often used:

$$Re_L = u_\infty L / \nu_\infty = \sqrt{Re_x} \qquad (10)$$

where length scale of boundary layer is defined as

$$L = \sqrt{\frac{\nu_\infty x}{u_\infty}}. \qquad (11)$$

The values of Re_L of the computational domain are from 207.9 to 1486.7. The computational domain is divided into 7 zones along streamwise direction with a total of 1506 grid points in the streamwise direction and 121 points in the wall-normal direction.

5.2.1 Mean flow

The mean pressure contours are shown in Fig. 5. As shown in the figure, there are a bunch of Mach waves emanating from the edge of the boundary layer. The angle between Mach line and x-direction is approximated as sum of tangential angle of edge of boundary layer and Mach angle, which is demonstrated in [25]. It is obvious that pressure is almost constant across the boundary layer and along the Mach lines. The distribution of pressure along the surface is shown in Fig. 6. As a result of interaction of inviscid external flow and viscous boundary layer flow, there are significant pressure gradients in streamwise direction especially in the upstream. This kind of interaction becomes weaker and weaker with the development of boundary layer. As a result, the Mach waves propagate to the downstream and strongly change the mean flow outside boundary layer in the downstream.

5.2.2 Disturbances in the flow field

To study the receptivity and stability of boundary layer, the boundary-layer instability waves are generated by controllable forcing disturbances. It is to be noted that the amplitude of forcing disturbance should be carefully chosen so that the nondimensionalized amplitude of perturbation is at least one-order larger than the maximum numerical noise, and it can not be too large to avoid the distortion of mean flow. The unsteady computations are carried out till the solutions reach a periodic state. After that, unsteady computations are conducted for one period in time. Temporal Fourier analysis is performed on the results of the unsteady flow in one period to obtain amplitude and phase angle of disturbances as follows,

$$\phi'(x, y, t) = |\phi'| e^{i[\psi'(x,y) - \omega t]}. \qquad (12)$$

4

Streamwise wavenumber can be extracted in DNS by using

$$\alpha_r = \frac{d|\psi'|}{dx} \tag{13}$$

$$\alpha_i = -\frac{1}{|\phi'|}\frac{d|\phi'|}{dx}. \tag{14}$$

Four different types of forcing disturbances are considered. These include: discrete eigenmodes forcing at the inflow, a blowing and suction slot imbedded in the wall surface, a narrow acoustic beam impinges on the leading-edge shock and plane freestream acoustic waves.

5.2.3 Forcing from the inlet

At inflow boundary, the flow is specified as the superposition of the steady base flow and a temporally periodical fluctuation of frequency ω, amplitude ϵ and streamwise wavenumber α as follows:

$$\phi(x_{in}, y, t) = \bar{\phi}(x_{in}, y, t) + \epsilon\hat{\phi}(y)e^{i(\alpha x - \omega t)}. \tag{15}$$

The disturbance structure contained in $\hat{\phi}(y)$ is obtained from LST results. The LST results of the first and second-mode unstable regions for Mach 4.5 flat-plate boundary layers, are shown in Fig. 7. Figure 7 shows that as the wave develops downstream, the second mode wave goes through a stable region of decay first, then a narrow unstable region of growth, followed by a stable region again afterward. The region of second mode instability predicted by LST is from $Re_L = 836$ (branch I neutral stability point) to 1028 (branch II neutral stability point). Figure 8 shows the contours of instantaneous normal velocity perturbation from numerical simulation after the flow field reaches a periodic state. This figure shows the performance of pure second-mode in the boundary layer. Figure 9 shows a local wave patterns in the second-mode growth region. It shows a typical second-mode wave pattern. The distribution of pressure perturbations along the surface is plotted in Fig. 10. The envelope (dash line) of the pressure perturbations shows the change of amplitude as the waves develop downstream. The amplitude of disturbance reaches the maximum at the branch II neutral point with $Re_L = \sqrt{Re_x} = 1056$ in results of the simulation. After passing the branch II neutral point, the amplitude of disturbance decays rapidly in the second-mode stable region. Finally, the disturbance dies out in the downstream.

From the numerical results of the unsteady solutions, the streamwise wavenumbers and growth rates of the disturbance can be computed. The wavenumbers and growth rates from numerical simulation are compared with the eigenvalues obtained from local linear stability analysis based on the same mean flow. Figure 11 and 12 show the comparison of streamwise wavenumbers and growth rates between the results from numerical simulation and LST respectively. In the figure, the real part and the imaginary parts of α are the wavenumbers and growth rates respectively. It shows that there is a good agreement between the results of simulation and and LST on α_r and α_i in the second-mode's unstable region, located in the region of $840 < Re_L < 1056$. We can also compare the eigenfunctions between the results from simulation and LST. Figure 13 shows the structure of velocity disturbance of simulation and LST calculations at the station $Re_L = 1007.57$. Despite the difference in the outside boundary layer, the agreement is remarkable. At this location, Reynolds number is large. Therefore, the nonparallel effect is small.

5.2.4 Forcing from the wall

In this test case, Unsteady flow develops naturally after disturbance are introduced by blowing and suction through a narrow slot imbedded in the wall surface near the leading edge. According to Balakumar and Malik's study [26], such forcing would generate several discrete modes as well as continuous spectra. The particular form of forcing used in the present study is

$$v_w(x) = A(x)\sin(\omega t) \tag{16}$$

where $A(x)$ is shown in Fig. 14. The nondimensional frequency of forcing disturbance equals to $F = 2.2 \times 10^{-4}$. After unsteady computations reach a periodic state, temporal Fourier analysis is performed to obtain amplitude and phase angle of perturbations of flow variables throughout the flow field. Figure 15 shows the contours of instantaneous pressure perturbation after the flow field reaches a periodic state. It is clear that blowing and suction introduce boundary layer disturbance as well as Mach waves radiation outside the boundary layer. The distribution of pressure perturbations along the surface is plotted in Fig. 16. The pressure perturbation on the wall is a combination of several wave modes near the blow and suction region. To study the receptivity of boundary layer to disturbance from blowing and suction, the induced perturbation in boundary layer are compared with pure second-mode waves. Here the amplitude of pure second-mode waves is adjusted by timing a factor so that the maximum value of pressure disturbance

5

on the wall surface equals to the amplitude of pressure disturbance from blowing and suction at the same location ($Re_L = 1056$). As the waves develop downstream reaching the branch I neutral stability point of the second mode, the amplitude of the second mode increases because of instability. In this region, the disturbances in the boundary layer are dominated by the second-mode waves, which is shown in Fig. 16. The second mode wave decays after passing through the branch II stability point and dies out very fast. We can also compare the structure of the induced disturbance in boundary layer with that of pure second-mode waves. Figure 17 and 18 show the structure of of normal velocity and temperature perturbations at the station $Re_L = 1056$. There is excellent agreement shown in the figure. There is also very good agreement when comparing structure of pressure or streamwise velocity perturbation, which are not plotted here.

5.2.5 Numerical accuracy

For the second-mode disturbances, the computational grids distribute 17 points in one wavelength. To examine the numerical accuracy, the computational grids are doubled in both streamwise and wall-normal directions. For refined grids, 3011 points are used in streamwise direction and 241 points are used in wall-normal direction. The simulation of boundary-layer disturbances due to blowing and suction is repeated on the refined grids. The comparison of perturbation amplitude of pressure along the wall between single grids and double grids is shown in Fig. 19. There is only tiny difference for disturbance amplitude in the downstream. The profiles of disturbance amplitude in the downstream located at $Re_L = 1200$ are also compared, which are shown in Figs. 20 and 21. It's obvious that refined grids can capture more sharp structures near the edge of boundary layer and Mach waves outside boundary layer. Because boundary-layer disturbances mainly concentrate inside boundary layer near the wall, the numerical simulation based on single grids can capture the structure of boundary-layer disturbances very well.

5.2.6 Receptivity to freestream acoustic waves

In the simulation, the freestream disturbances are superimposed on the steady mean flow to investigate the development of boundary-layer instability waves with the effects of the bow shock interaction. The freestream disturbances are assumed to be weak monochromatic planar acoustic waves. The perturbations of flow variable introduced by the freestream acoustic wave before

reaching the bow shock can be written in the following form:

$$\left\{ \begin{array}{c} u' \\ v' \\ p' \\ \rho' \end{array} \right\}_\infty = \left\{ \begin{array}{c} |u'| \\ |v'| \\ |p'| \\ |\rho'| \end{array} \right\}_\infty e^{i[k_x\,x + k_y\,y - \omega t]} \quad (17)$$

where $|u'|$, $|v'|$, $|p'|$, and $|\rho'|$ are perturbation amplitudes satisfying the following relations:

$$|u'|_\infty = u_\infty \epsilon k_x / k \,, \qquad |v'|_\infty = u_\infty \epsilon k_y / k$$
$$|p'|_\infty = \rho_\infty C_\infty |u'| \,, \qquad |\rho'|_\infty = |p'|_\infty / C_\infty^2$$

where ϵ represents the freestream wave magnitude, which is a small number. The parameter k is the freestream wavenumber with components k_x and k_y in streamwise and normal direction respectively,

$$k_x = k \cos(\theta_{ac}), \qquad k_y = -k \sin(\theta_{ac}), \quad (18)$$

where θ_{ac} is the orientation angle of acoustic wave relative to streamwise direction (see Fig. 22). The wavenumber is related to the circular frequency ω by:

$$\omega = k\,(c_\infty + u_\infty \cos \theta_{ac}) \quad (19)$$

5.2.7 Plane acoustic wave with zero angle

In this case, a plane acoustic wave with frequency of $F = 2.2 \times 10^{-4}$ and zero angle is allowed to enter the top computational boundary. From references [27,28], the forced acoustic disturbances penetrate the boundary layer and form the Stokes waves, which can induce inherent homogeneous discrete modes of boundary layer. To study the performance of Stokes wave in boundary layer, the computational domain is extended to $x = 0.5m$. Figures 22 and 23 shows the contours of pressure perturbation after the unsteady calculation reaching periodic state. From the results in section 5.2.3 and 5.2.4, the secnod-mode disturbances are expected to be dominant ranging from $x = 0.1$ ($Re_L = 848.5$) to $x = 0.2$ ($Re_L = 1200$). However, there are no dominant secnod-mode disturbances shown in this range (Fig. 23). Fig. 24 gives the the distribution of pressure perturbations along the wall surface. In the downstream outside the second-mode unstable region, another unstable mode comes out. From LST, all discrete modes are stable at the forcing frequency $F = 2.2 \times 10^{-4}$ when $Re_L > 1200$

6

$(x = 0.2m)$. The dominant disturbances in the downstream are Stokes waves. The wavenumber is calculated based on pressure perturbation by using temporal Fourier analysis and Equ. 14, which is shown in Fig. 25. It shows that the wavenumber in the downstream $(x > 0.2m)$ is almost constant $(\alpha_r = 1350/m)$ due to the dominance of Stokes waves. The corresponding phase velocity based on this constant wavenumber is $1 + 1/M_\infty$ after being normalized by freestream velocity. In the second-mode unstable region, the secnod-mode disturbances are modulated by Stokes waves. In order to decompose the different components containing in boundary layer disturbances, spatial Fourier analyses are performed for different zones of computational domain. In spatial frequency (wavenumber) domain, the amplitude of of pressure disturbances in different zones is shown in Fig. 26. There is only one peak when the computational zone is located in downstream after $x > 0.2m$. There are two peaks in the zones including the second-mode unstable region (Zone 5 and Zone 6), and one of them results from the components of Stokes waves. The upper peak with larger wavenumber is centred at $18001/m$ and corresponding phase velocity is $1 - 1/M_\infty$. A bandpass filter window is put upon the upper peak and lower peak to obtain second-mode disturbances and Stokes waves respectively. Figure 27 shows the wave components related to the lower peak and 28 shows the wave pattern from the upper peak. The wave shown in Fig. 27 is Stokes wave. The wave shape showed in Fig. 28(b) is very similar to that in Fig. 10, and it is demonstrated to be second-mode disturbances. To confirm this conclusion, spatial Fourier analyses and the decomposition scheme through filter window are conducted on whole computational domain. The structures of decomposed second-mode disturbances from total boundary-layer disturbances can match that of pure second-mode disturbances that are forced at inflow and propagating downstream to the same location. It is found that the filter and spatial Fourier analysis can successfully decompose the different components in boundary-layer disturbances for this case. To compare to the typical structure of second-mode disturbances and Stokes waves, the profiles of second-mode waves at $Re_L = 1056$ (Branch II neutral point) and profiles of Stokes waves at $Re_L = 1614$ are plotted in Figs. 29 and 30. While the maximum temperature disturbances occur near the edge of boundary layer for second-mode disturbances, the peak temperature perturbation happens on the wall surface for the Stokes waves.

To quantitatively study the acoustic receptivity of boundary layer, the receptivity coefficient in this paper is defined as

$$K_s = |p'_{II}|/|p'_\infty|, \qquad (20)$$

where $|p'|_{II}$ is the amplitude of pressure perturbation at Branch II neutral point. For receptivity to plane acoustic wave with zero angle, the receptivity coefficient is 1.03 based on above definition.

From above analyses, the freestream acoustic wave can induce discrete boundary-layer modes as well as Stokes waves. The Stokes waves are considerably amplified in the boundary layer. The expected dominance of high-frequency second-mode instabilities were not detected in the experiments by Kendall [24] ($Mach = 4.5$). In the experiment, the boundary-layer disturbances were generated by freestream acoustic waves radiated from tunnel wall turbulence. From the results of simulation, the receptivity coefficient at Branch II of second-mode neutral point is close to one at the frequency considered in this case. Thus, if the amplitude of freestream acoustic wave at high frequency in second-mode unstable band is very small, the induced second-mode wave is not detectable. Another reason is due to the modulation of induced second-mode disturbances by Stokes waves. The observed strongly-unstable band lying at frequencies above the second-mode one for sound-induced waves on cones at hypersonic speed [29] may be explained with amplification of Stokes waves. Further research work is needed to study the performance of Stokes waves induced by freestream acoustic waves.

5.2.8 A beam of acoustic waves with different angles

A beam of acoustic waves enter the flow field through a slot on the shock boundary. Seven different orientation angles of acoustic waves evenly spanned between $0°$ and $90°$ are considered respectively. Figure 31 shows the contours of pressure perturbation due to freestream acoustic waves with $\theta_{ac} = 90°$. It shows that a bunch of transmitted acoustic waves enter the flow field through a slot on the shock boundary. The transmitted acoustic waves propagate downstream and impinge the wall, which resulting in a bunch of reflected acoustic waves. It shows that the interaction of acoustic waves and boundary layer generate boundary-layer disturbances, which contain discrete-mode instability waves and Stokes waves. Spatial Fourier analyses and band-pass filter window are used to decompose second-mode waves from the total boundary-layer disturbances. The receptivity coefficient based on definition of Equ. 20 is 0.29 when $\theta_{ac} = 90$. Such analyses and decomposition technique are also used in other cases with different acoustic wave angles. Figure 32 shows the receptivity coefficients changing with the different acoustic angles. The maximum receptivity coefficient is obtained when the acoustic angle $\theta_{ac} = 15°$,

7

while the minimum receptivity occurs at $\theta_{ac} = 75°$. At $Mach = 4.5$, the Mach angle is 12.8° and the shock angle ranges from 16.3° to 13.8° from the results of simulation. The curve of receptivity coefficient changing with the angle of acoustic waves shows that maximum receptivity is obtained when the freestream acoustic waves propagate in the direction parallel to the Mach line, and minimum receptivity occurs when the freestream acoustic waves propagate in the direction normal to Mach line or shock wave.

6   Receptivity and Stability of Reacting O_2 Flow over a Flat Plate

The real gas effect on receptivity and stability of hypersonic flow is studied by simulation of a Mach 10 oxygen flow over a flat plate in both perfect gas and thermochemically nonequilibrium regime. The specific flow conditions are:

$$M_\infty = 10 \qquad\qquad T_\infty = 350.0\,K$$
$$p_\infty = 3903.5\,Pa \qquad\qquad Pr = 0.72$$
$$Re_\infty = \rho_\infty U_\infty / \mu_\infty = 6.6 \times 10^6 / m$$

The computational domain ranges from $x = 0.01$ ($Re_x = 6.6 \times 10^5$) to $x = 0.483$ ($Re_x = 3.19 \times 10^6$). The computational domain is divided into 9 zones along streamwise direction with a total of 2181 grid points and 121 points in the wall-normal direction.

6.1   Mean Flow

Figure 33 shows the contours of pressure and Fig. 34 shows contours of mass fraction of dissociated oxygen. It obvious that there is a bunch of Mach waves emanating from the edge of the boundary layer and significant the dissociation which mainly takes place in the vicinity of the wall surface. Compared with Mach = 4.5 case, the shock is pushed more close to the wall.

The wall temperature of base flow is shown in Fig 35. The wall temperature is almost constant for perfect gas while the vibrational temperature is in nonequilibrium with translational temperature in reacting flow. The profile of temperature located at $x = 0.117m$ is shown in Fig 36. temperature in reacting flow. Wall temperature of nonequilibrium flow is much lower than that of perfect gas flow because the reaction is endothermic. As a result, the thickness of boundary layer for perfect gas is larger than reacting flow, which may change

the property of the most amplified second mode disturbance because the wavelength of second mode is proportional to boundary layer thickness [30]. In this case, the maximum mass fraction of dissociated O_2 is 7%, which occurs on the wall near the outlet.

6.2   Neutral Curve of Stability

Before introducing disturbances, the stability properties are studied by LST in perfect regime. The stability neutral curve is plotted in Fig 37. It shows that the first-mode neutral curve and the second-mode neutral curve merge together. Base on this neutral curve, different sources of disturbances with nondimensional frequency of $F = 0.8125 \times 10^{-4}$ or $F = 0.5 \times 10^{-4}$ are introduced to flow field to study the receptivity and stability of nonequilibrium hypersonic flow.

6.3   Forcing from the Wall

Disturbances are introduced by blowing suction through a slot embedded on the wall surface near the leading edge. The form of blowing and suction is controlled by Equ. 16 and the shape is similar to that shown in Fig. 14.

6.3.1   Blowing and Suction at Frequency $F = 0.8125 \times 10^{-4}$

Figures 38 and 39 show the contours of pressure perturbation for perfect gas and reacting flow respectively. From the structure of pressure disturbances near the wall, it shows that there is an inter-mode change for boundary-layer instability waves near the location $x = 0.1m$. This is also shown in Fig. 40. Compared with perfect gas flow, the unstable region of nonequilibrium flow is longer and the peak amplitude is larger. In other worlds, the real gas effect is destabilizing for the discrete modes in this region. The decomposition of discrete modes of boundary-layer disturbances induced by blowing and suction is still ongoing. The forcing disturbances generate boundary-layer instability waves as well as Mach waves (Fig. 39). The Mach waves propagate alone the Mach line and lead to the oscillation of shock wave. The pressure perturbation behind the shock is shown in Fig. 41. In this case, there is no freestream disturbances, so the pressure perturbation results from the oscillation of shock. The amplitude of pressure perturbation behind the shock is a little bit larger for perfect gas than that for nonequilibrium flow.

8

For perfect flow, second-mode disturbances forced from the inlet are also studied and compared with the results from blowing and suction. The amplitude of pure second-mode waves is adjusted by timing a factor so that the maximum value of pressure disturbance on the wall surface equals to the amplitude of pressure disturbance from blowing and suction at the same location ($Re_L = 1010$), which is shown in Fig. 42. In the downstream after $Re_L > 1010$, there is good agreement in comparison. The profiles of disturbances from blowing and suction agree very well with the second-mode structure. Therefore, the induced boundary-layer disturbances are second-mode dominant at this location.

6.3.2 Blowing and Suction at Frequency $F = 0.5 \times 10^{-4}$

Figures 43 and 44 show the contours of pressure perturbation for perfect gas and reacting flow respectively. The inter-mode change occurs near the location $x = 0.3m$. This is also shown in Fig. 45. Again, the unstable region for nonequilibrium flow is longer and the peak amplitude is larger, which means that the real gas effect is destabilizing for the discrete modes in this region.

For perfect flow, first-mode disturbances forced from the inlet are also studied and compared with the results from blowing and suction. The amplitude of pure discrete-mode waves is adjusted by timing a factor so that the maximum value of pressure disturbance on the wall surface equals to the amplitude of pressure disturbance from blowing and suction at the same location ($Re_L = 1570.5$) (Fig. 46) There is good agreement in comparison for amplitude of pressure perturbation in downstream.

6.3.3 Receptivity to Freestream Acoustic Waves

In this case, a plane acoustic wave with frequency of $F = 0.5 \times 10^{-4}$ and zero angle is allowed to enter the top computational boundary. The receptivity of boundary layer is studied for both nonequilibrium and perfect gas with the same freestream conditions. Figures 47 and 48 show the contours of pressure perturbation for perfect gas and reacting flow respectively. The transmitted acoustic waves behind the shock are concentrated outside boundary layer. The transmitted acoustic waves induce different modes of boundary-layer disturbances, which are dominant inside boundary layer. There is inter-mode change near the location $x = 0.3m$. This is also shown in Fig. 49. Again, it

shows that the real gas effect is destabilizing for the discrete modes in the down stream region after $x > 0.3m$.

Spatial Fourier analysis is performed on pressure perturbation on the wall and the results are shown in spatial frequency (wavenumber) domain (Fig. 50). Unlike Mach 4.5 case, there are no separated peaks shown in the figure, therefore, filter window doesn't work to decompose the different components in boundary-layer disturbances. Some other techniques are required for decomposition of different components in boundary layer disturbances.

7 Conclusions

The results from TVD method are used as inflow conditions to commence numerical simulation of hypersonic flow over flat plates by using shock-fitting method, which are validated by comparing the numerical results with experimental results. The receptivity coefficient for flow over a flat plat at $Mach 4.5$ to plane acoustic waves at zone angle is close to 1. The receptivity to acoustic wave at different angles shows that the receptivity coefficient reaches maximum when the freestream acoustic waves propagate along the Mach line, and it approaches minimum value when the freestream acoustic waves propagate in the direction normal to Mach line or shock wave. The receptivity and stability of a Mach 10 oxygen flow over a flat plate is studied in both perfect gas and thermochemically nonequilibrium regime. Compared with results of perfect gas, the unstable region for nonequilibrium flow is longer and the peak amplitude is larger, which means that the real gas effect is destabilizing for the discrete modes in this region for the frequencies considered in this study.

8 Acknowledgements

References

[1] Th. Herbert. Secondary Instability of Boundary Layers. *Annual Review of Fluid Mechanics*, Vol. 20, pp. 487-526, 1988.

[2] A. M. O. Smith and N. Gamberoni. Transition, Pressure Gradient and Stability Theory. *Douglas*

Aircraft Co., El Segundo, California, Rept. ES 26388, 1956.

[3] J. L. Van Ingen. A Suggested Semi-Empirical Method for the Calculation of Boundary Layer Transition Region. *University of Techn., Dept. of Aerospace Eng., Delft*, Rept. UTH-74, 1956.

[4] P. Krogmann. An experimental study of boundary layer transition on a slender cone at mach 5. In *Symposium on Laminar-Turbulent Transition*. AGARD-CP-224, 1977.

[5] I. E. Beckwith. Development of a High Reynolds Number Quiet Tunnel for Transition Research. *AIAA Journal*, Vol. 13, 1975.

[6] S. R. Pate and C. J. Schueler. Radiated Aerodynamic Noise Effects on Boundary-Layer Transition in Supersonic and Hypersonic Wind Tunnels. *AIAA Journal*, Vol. 7, pp. 450, 1969.

[7] S. R. Pate. Measurements and Correlation of Transition Reynolds Numbers on Sharp Slender Cones at High Speeds. *AIAA Journal*, Vol. 9, pp. 1082, 1971.

[8] J. L. Potter and J. D. Whitfield. Effects of Slight Nose Bluntness and Roughness on Boundary-Layer Transition in Supersonic Flows. *Journal of Fluid Mechanics*, Vol. 12, part 4, pp. 501–535, 1962.

[9] J. L. Potter. Observations on the Influence of Ambient Pressure on Boundary-Layer Transition. *AIAA Journal*, Vol. 6, pp. 1907, 1968.

[10] F. K. Owen P. C. Stainback, R. D. Wagner and C. C. Horsman. *Experimental Studies of Hypersonic Boundary-Layer Transition and Effects of Wind Tunnel Disturbances*. NASA TN D-1974, 1974.

[11] E. J. Softly, B. C. Graber, and R. C. Zempel. Experimental Observation of Transition of the Hypersonic Boundary Layer. *AIAA Journal*, Vol. 7, No. 2, pp. 257-263 1969.

[12] K. F. Stetson, E. R. Thompson, J. C. Donaldson, and L. G. Siler. Laminar Boundary Layer Stability Experiments on a Cone at Mach 8, Part 4: on Unit Reynolds Number and Environmental Effects. *AIAA paper 86-1087*, 1986.

[13] M. Nishioka and M. V. Morkovin. Boundary-Layer Receptivity to Unsteady Pressure Gradients: Experiments and Overview. *Journal of Fluid Mechanics*, Vol. 171, pp. 219-261 1986.

[14] M. E. Goldstein and L. S. Hultgren. Boundary-Layer Receptivity to Long-Wave Free-Stream Disturbances. *Annual Review of Fluid Mechanics*, Vol. 21, pp. 137-166 1989.

[15] W. S. Saric, H. L. Reed, and E. J. Kerschen. Leading edge receptivity to sound: Experiments, dns, and theory. *AIAA Paper 94-2222*, 1994.

[16] C. Park. *Nonequilibrium Hypersonic Aerothermodynamics*. Wiley Interscience, 1990.

[17] C. Park. Review of chemical-kinetic problems of future nasa missions, i: Earth entries. *Journal of Thermophysics and Heat Transfer*, 7:385–398, 1993.

[18] Y. Ma and X. Zhong. Numerical simulation of transient hypersonic flow with real gas effects. AIAA Paper 99-0416, AIAA, 1999.

[19] X. Zhong. High-Order Finite-Difference Schemes for Numerical Simulation of Hypersonic Boundary-Layer Transition. *Journal of Computational Physics*, 144:662–709, 1998.

[20] X. Zhong. Additive Semi-Implicit Runge-Kutta Schemes for Computing High-Speed Nonequilibrium Reactive Flows. *Journal of Computational Physics*, Vol. 128, pp. 19-31, 1996.

[21] T. Gökçen. *The Computation of Hypersonic Low Density Flows with Thermochemical Nonequilibrium*. PhD thesis, Stanford University, 1989.

[22] J. M. Kendall. An Experimental Investigation of Leading-Edge Shock-Wave- Boundary-Layer Interation at Mach5.8. *Journal of the Aeronautical Sciences*, pp. 47–56, 1957.

[23] X. Zhong and T. Lee. Nonequilibrium Real-Gas Effects on Disturbance/Bow Shock Interaction in Hypersonic Flow Past a Cylinder. *AIAA paper 96-1856*, June 1996.

[24] J. M. Kendall. Wind Tunnel Experiments Relating to Supersonic and Hypersonic Boundary-Layer Transition. *AIAA Journal*, Vol. 13, No. 3, pp. 290–299, 1975.

[25] Y. Ma and X. Zhong. Direct numerical simulation of instability of nonequilibrium reacting hypersonic boundary layers. AIAA Paper 2000-0539, AIAA, 2000.

[26] P. Balakumar and M.R. Malik. Discrete modes and continuous spectra in supersonic boundary layers. *Journal of Fluid Mechanics*, 239:631–656, 1992.

10

[27] L. M. Mack. Linear Stability Theory and the Problem of Supersonic Boundary-Layer Transition. *AIAA Journal*, Vol. 13, No. 3, pp. 278-289, 1975.

[28] S. A. Gaponov. Interaction of supersonic boundary layer with acoustic disturbances. *Fluid Dynamics (Translated From Russian)*, (6):51–56, 1977.

[29] J. M. Kendall. Some Comparisons of Linear Stability Theory with Experiment at Supersonic and Hypersonic Speed. *Instability and Transition, Vol. I*, M. Y. Hussaini and R. G. Viogt, editors, pp. 217-232, Springer-Verlag, 1990.

[30] M. L. Hudson, N. Chokani, and G. V. Candler. Nonequilibrium effects on hypersonic boundary layers and inviscid stability. *AIAA Paper 94-0825*, 1994.
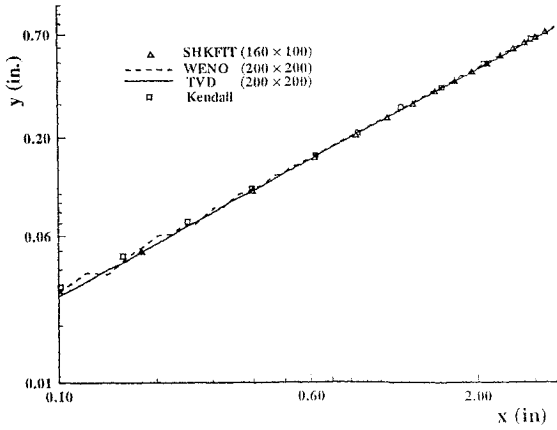
Figure 1: Location of shock wave at $M_\infty = 5.79$.
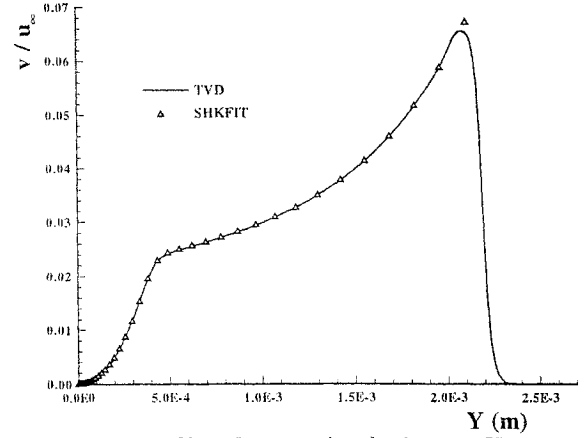
Figure 4: Profile of normal velocity at $X = 0.007m$ and $M_\infty = 4.5$.
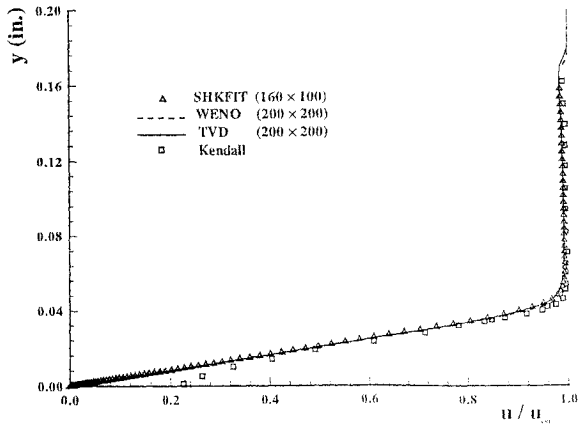
Figure 2: Profile of streamwise velocity at $X = 0.64inch$ $(M_\infty = 5.79)$
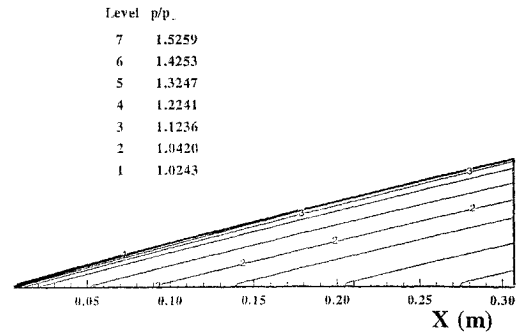
Figure 5: Pressure contours of mean flow at $M_\infty = 4.5$ by shock-fitting method.
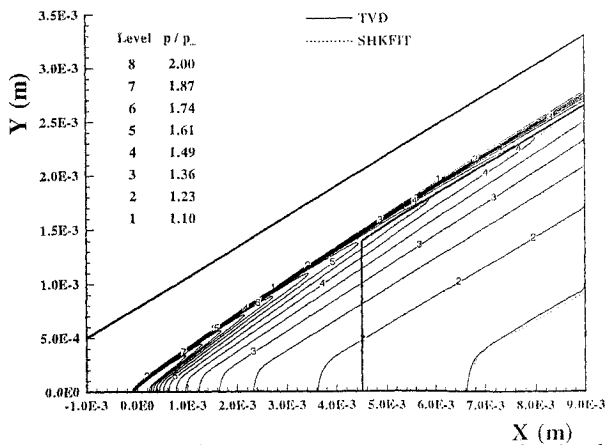
Figure 3: Steady pressure contours near the leading edge at $M_\infty = 4.5$.
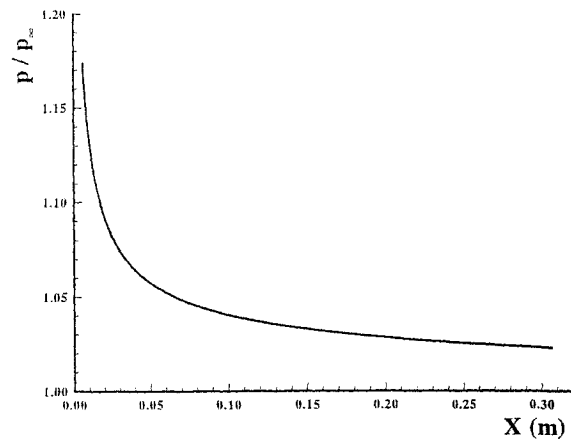
Figure 6: Distribution of pressure along the plate surface at $M_\infty = 4.5$.
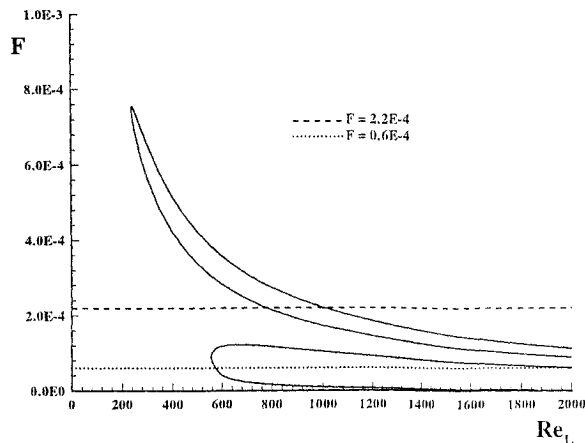
Figure 7: Neutral curves of stability (F vs. Re_L) for two-dimensional first- and second-mode disturbances at $M_\infty = 4.5$.
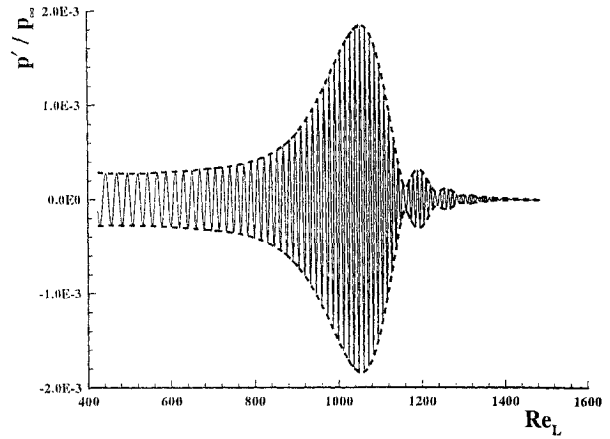
Figure 10: Distribution of pressure perturbation along the wall surface at $M_\infty = 4.5$, $F = 2.2 \times 10^{-4}$.
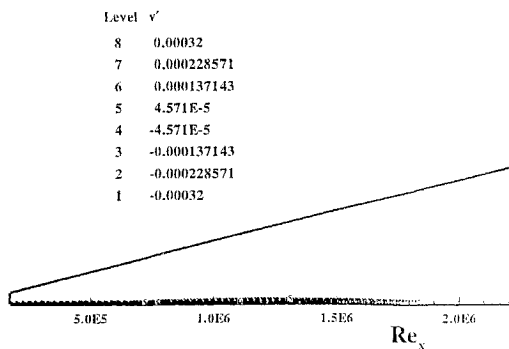
Figure 8: Instantaneous normal velocity perturbation contours; at $M_\infty = 4.5$, $F = 2.2 \times 10^{-4}$.
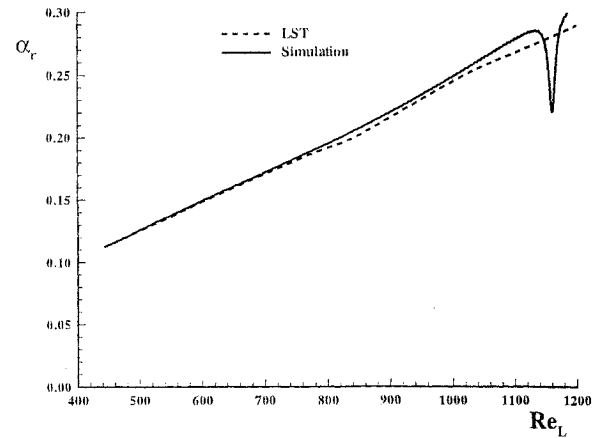
Figure 11: Comparison of streamwise wavenumber obtained by simulation and LST calculation respectively at $M_\infty = 4.5$, $F = 2.2 \times 10^{-4}$.
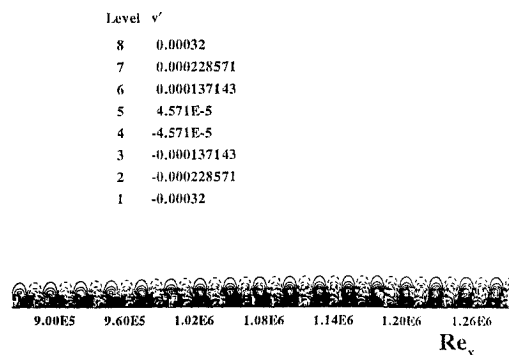
Figure 9: Local patterns of instantaneous normal velocity perturbation contours; at $M_\infty = 4.5$, $F = 2.2 \times 10^{-4}$.
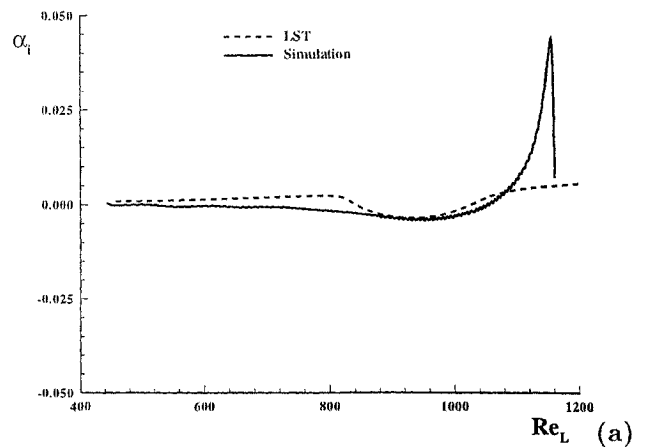
Figure 12: Comparison of growth rates between simulation and LST calculation at $M_\infty = 4.5$, $F = 2.2 \times 10^{-4}$

13
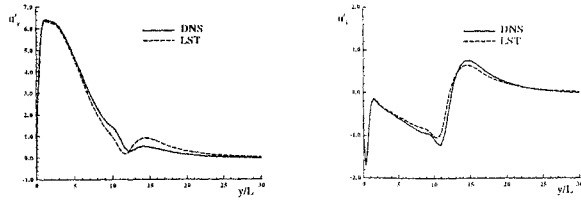
Figure 13: Comparison of structure of eigenfunctions at $M_\infty = 4.5$, $Re_L = 1007.57$, and $F = 2.2 \times 10^{-4}$.
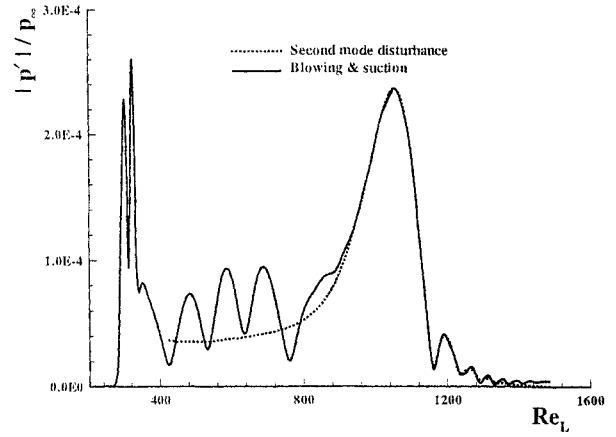
Figure 16: Comparison of amplitude of pressure perturbation along the wall surface at $M_\infty = 4.5$, $F = 2.2 \times 10^{-4}$.
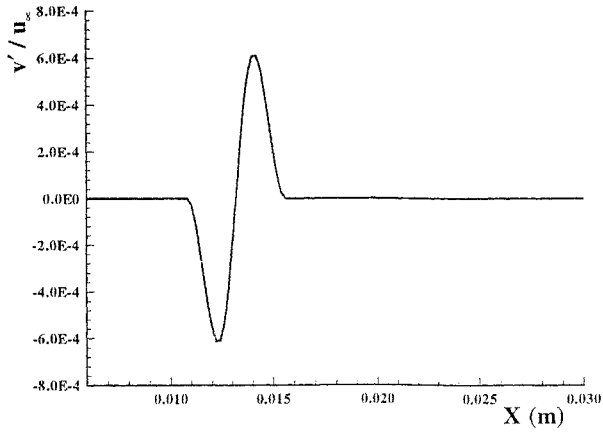
Figure 14: Vertical velocity distribution over blowing and suction slot for generating disturbances.
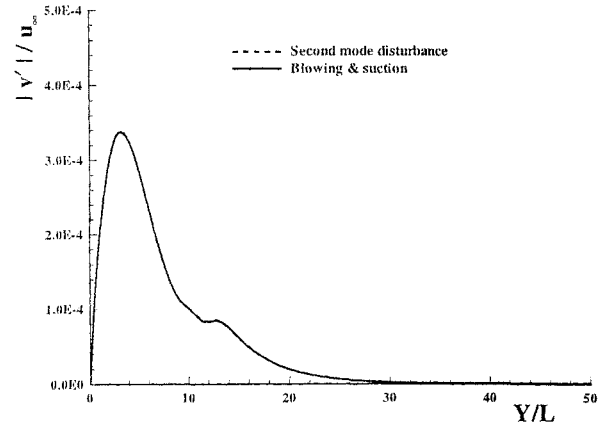
Figure 17: Structure of temperature disturbance at $M_\infty = 4.5$, $F = 2.2 \times 10^{-4}$, $Re_L = 1056$.
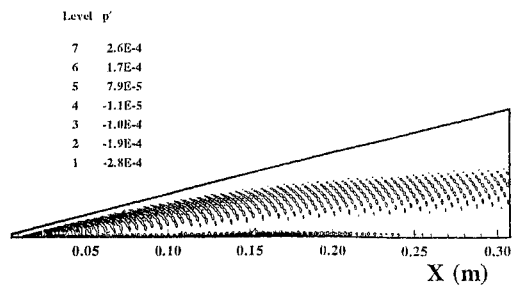
Figure 15: Contours of pressure perturbation due to blowing and suction at $M_\infty = 4.5$, $F = 2.2 \times 10^{-4}$.
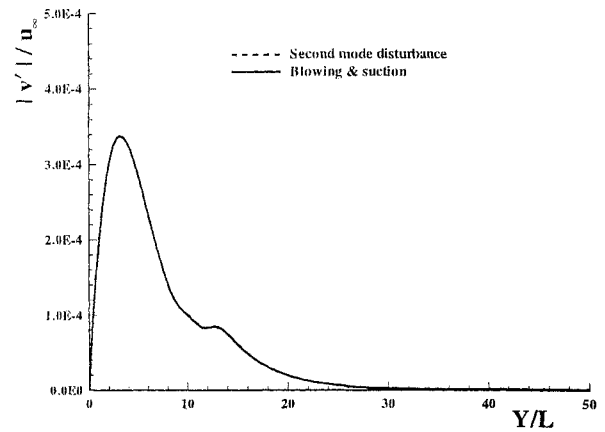
Figure 18: Structure of normal velocity disturbance at $M_\infty = 4.5$, $F = 2.2 \times 10^{-4}$, $Re_L = 1056$.

14
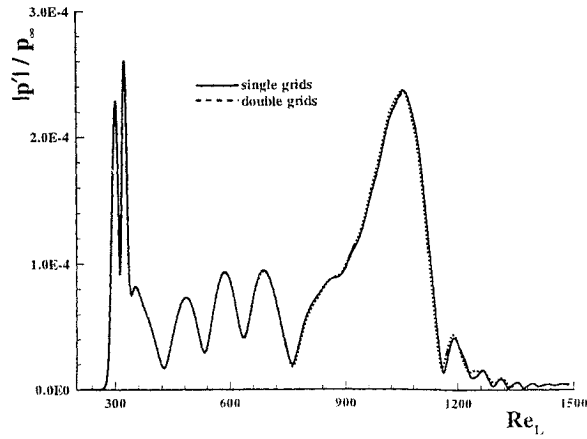
Figure 19: Comparison of amplitude of pressure perturbation calculated on different computational grids $(M_\infty = 4.5, F = 2.2 \times 10^{-4})$.
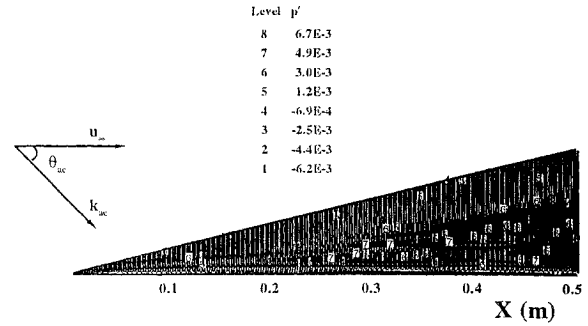
Figure 22: Instantaneous pressure perturbation contours due to a plane acoustic wave with zero angle $(M_\infty = 4.5, F = 2.2 \times 10^{-4})$.
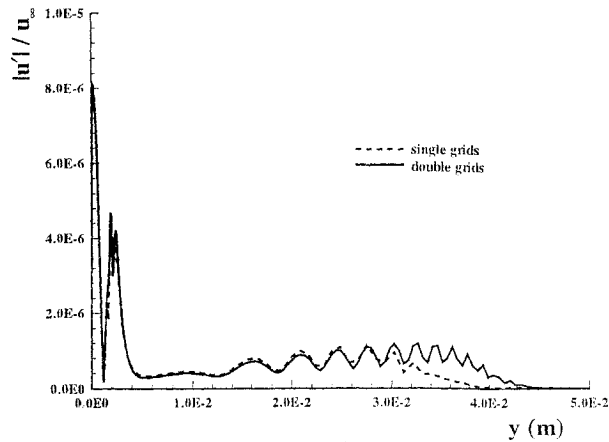
Figure 20: Structure of amplitude of streamwise velocity perturbation calculated on different computational grids $(M_\infty = 4.5, F = 2.2 \times 10^{-4}, Re_L = 1200)$.
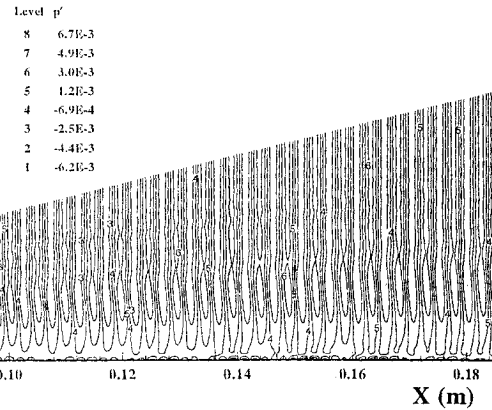
Figure 23: Instantaneous pressure perturbation contours due to a plane acoustic wave with zero angle near the wall $(M_\infty = 4.5, F = 2.2 \times 10^{-4})$.
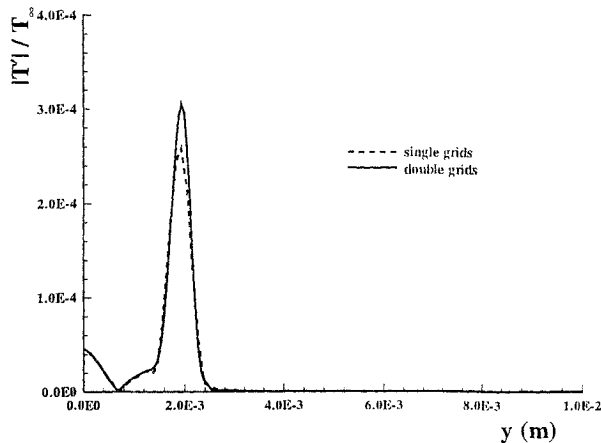
Figure 21: Structure of amplitude of temperature perturbation calculated on different computational grids $(M_\infty = 4.5, F = 2.2 \times 10^{-4}, Re_L = 1200)$.
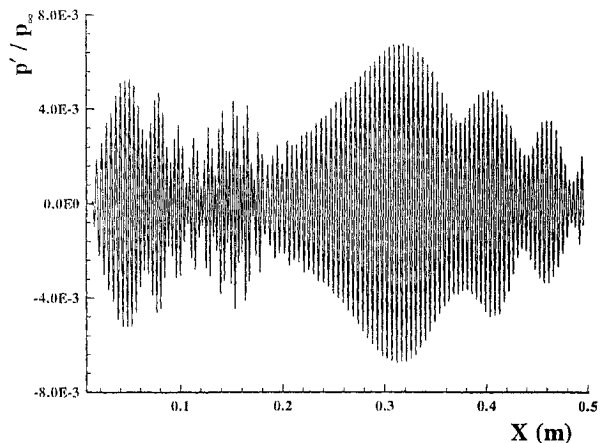
Figure 24: Pressure perturbation along the wall surface due to a plane acoustic waves with zero angle $(M_\infty = 4.5, F = 2.2 \times 10^{-4})$.

15
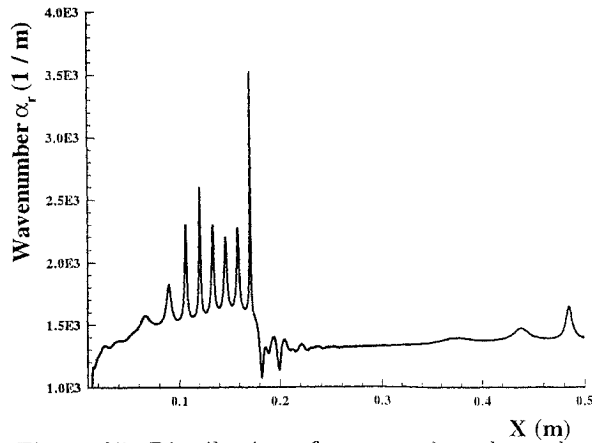
Figure 25: Distribution of wavenumber along the wall surface ($M_\infty = 4.5$, $F = 2.2 \times 10^{-4}$).
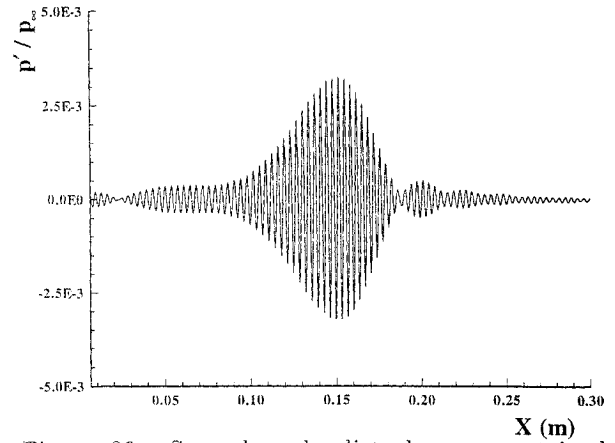
Figure 28: Second-mode disturbances contained in boundary-layer disturbances for pressure perturbation along the wall surface due to a plane acoustic waves with zero angle. ($M_\infty = 4.5$, $F = 2.2 \times 10^{-4}$).
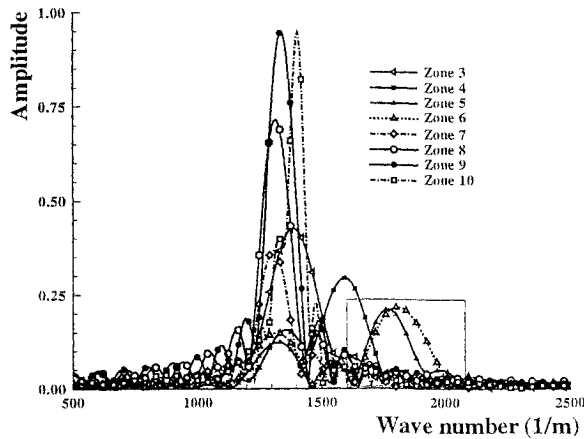
Figure 26: Amplitude of pressure perturbation in spatial frequency domain ($M_\infty = 4.5$, $F = 2.2 \times 10^{-4}$).
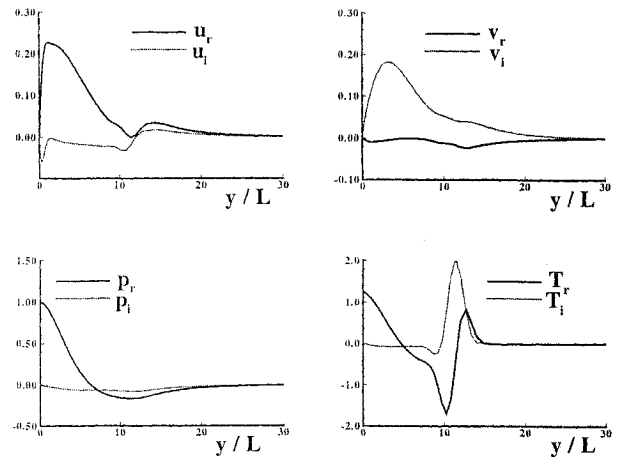
Figure 29: The structure of second-mode disturbances at $Re_L = 1056$ ($M_\infty = 4.5$, $F = 2.2 \times 10^{-4}$).
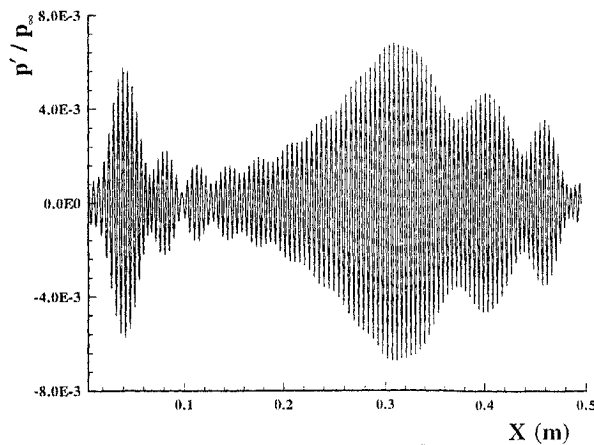
Figure 27: Stokes waves contains in boundary-layer disturbances for pressure perturbation along the wall surface due to a plane acoustic waves with zero ($M_\infty = 4.5$, $F = 2.2 \times 10^{-4}$).
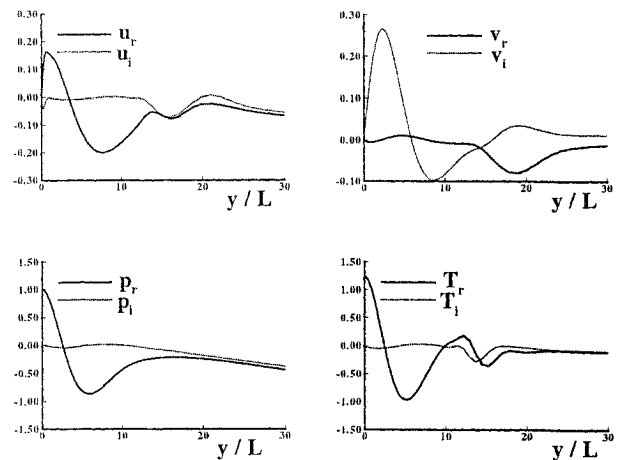
Figure 30: The structure of Stokes waves at $Re_L = 1614$ ($M_\infty = 4.5$, $F = 2.2 \times 10^{-4}$).

16
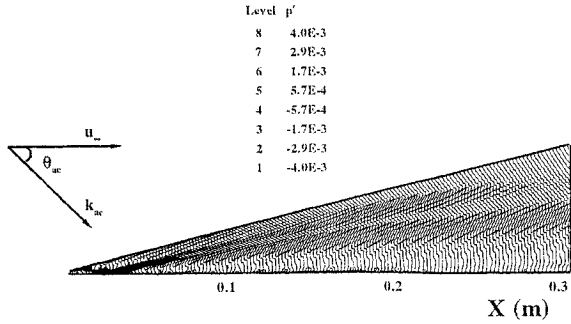
Figure 31: Contours of pressure perturbation due to a beam of acoustic waves at $\theta_{ac} = 90°$;
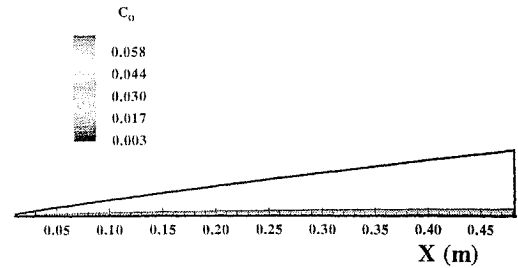
Figure 34: The contours of mass fraction of dissociated oxygen for nonequilibrium O_2 flow over a flat plate at $M_\infty = 10$.
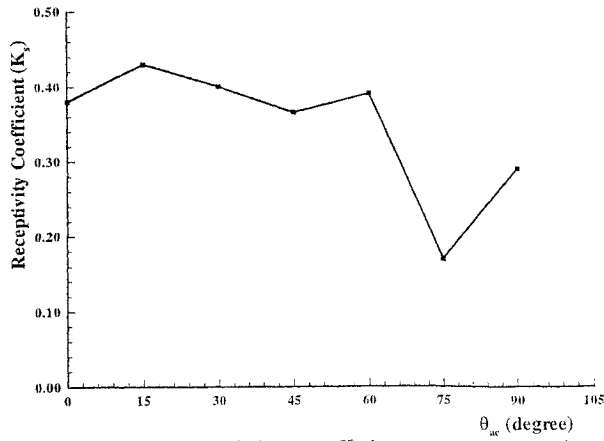
Figure 32: Receptivity coefficients over acoustic wave at different angles. ($M_\infty = 4.5$, $F = 2.2 \times 10^{-4}$).
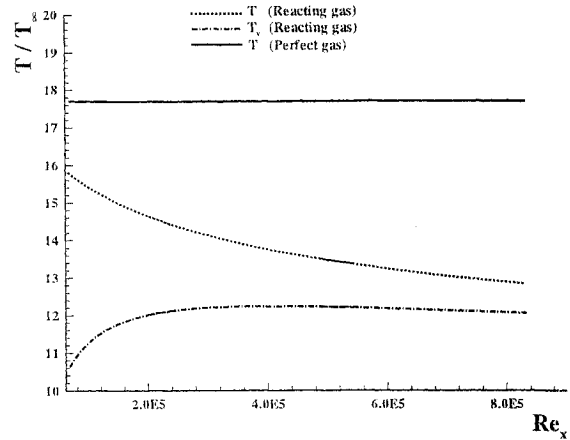
Figure 35: Comparison of wall temperature between perfect gas flow and noequilibrium flow at $M_\infty = 10$.
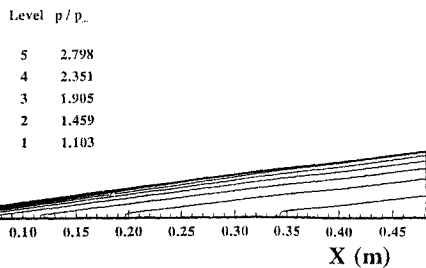
Figure 33: The contours of pressure for nonequilibrium O_2 flow over a flat plate at $M_\infty = 10$.
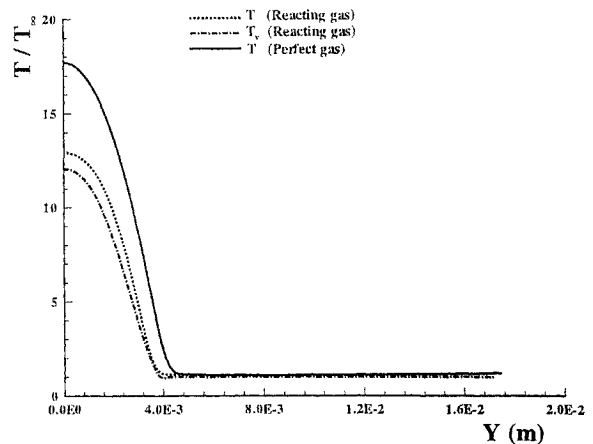
Figure 36: Profiles of mean temperature at $M_\infty = 10$, $x = 0.117m$.

17
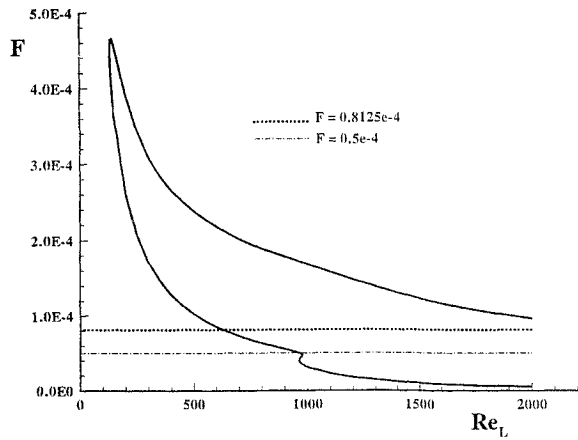
Figure 37: Neutral curves of stability (F vs. Re_L) for two-dimensional disturbances at $M_\infty = 10$.
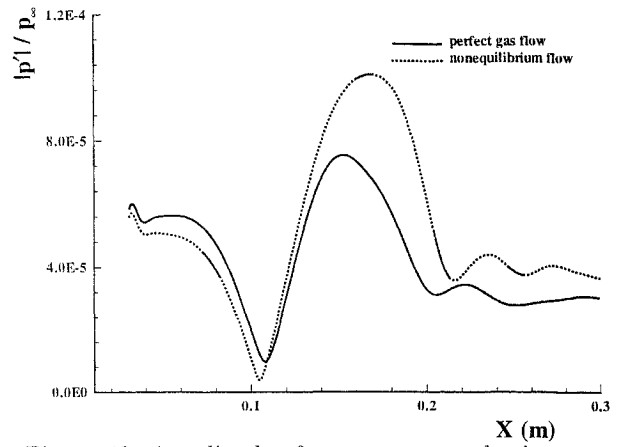
Figure 40: Amplitude of pressure perturbations on the wall due to blowing and suction at $M_\infty = 10$, $F = 0.8125 \times 10^{-4}$.
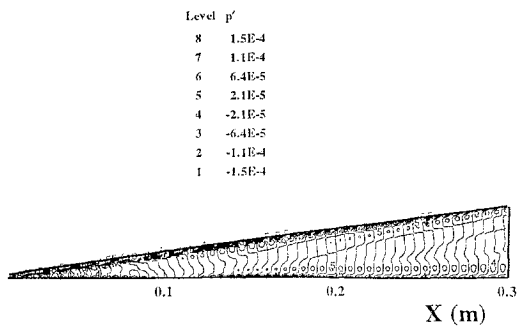
Figure 38: Instantaneous contours of pressure perturbations due to blowing and suction for perfect gas at $M_\infty = 10$, $F = 0.8125 \times 10^{-4}$.
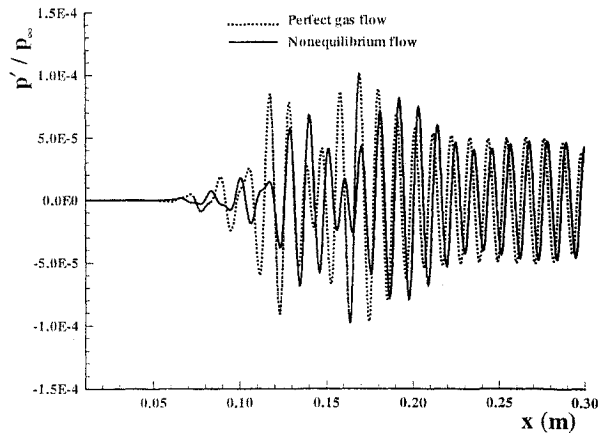
Figure 41: Pressure perturbation behind the shock due to blowing and suction at $M_\infty = 10$, $F = 0.8125 \times 10^{-4}$.
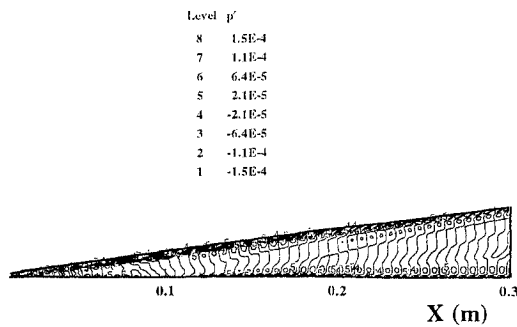
Figure 39: Instantaneous contours of pressure perturbations due to blowing and suction for nonequilibrium flow at $M_\infty = 10$, $F = 0.8125 \times 10^{-4}$.
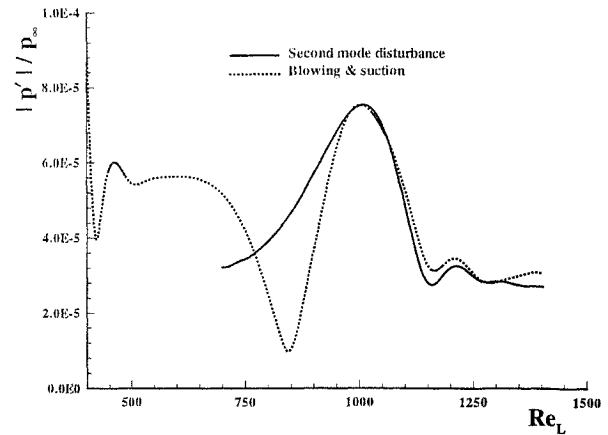
Figure 42: Comparison of amplitude of second-mode disturbance on the wall induced by blowing and suction and that of pure second-mode developed from inlet at $M_\infty = 10$, $F = 0.8125 \times 10^{-4}$.

18

Level p'
8   1.9E-4
7   1.3E-4
6   8.0E-5
5   2.6E-5
4   -2.8E-5
3   -8.2E-5
2   -1.4E-4
1   -1.9E-4
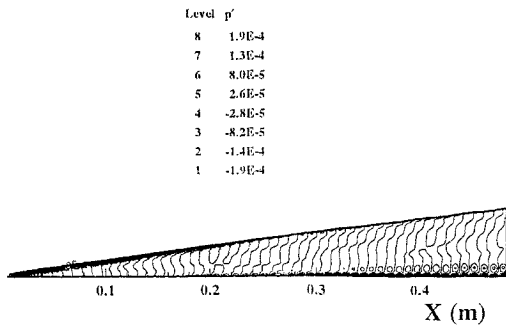
Figure 43: Instantaneous contours of pressure pertur-bations due to blowing and suction for perfect gas at $M_\infty = 10$, $F = 0.5 \times 10^{-4}$.

Figure 46: Comparison of amplitude of second-mode disturbance on the wall induced by blowing and suction and that of pure second-mode developed from inlet at $M_\infty = 10$, $F = 0.5 \times 10^{-4}$.

Level p'
8   1.9E-4
7   1.3E-4
6   8.0E-5
5   2.6E-5
4   -2.8E-5
3   -8.2E-5
2   -1.4E-4
1   -1.9E-4
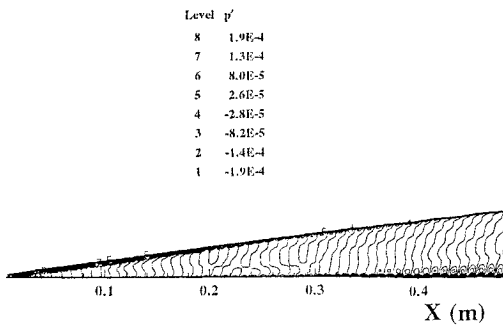
Figure 44: Instantaneous contours of pressure pertur-bations due to blowing and suction for nonequilibrium flow at $M_\infty = 10$, $F = 0.5 \times 10^{-4}$.

Level p'
8   3.1E-2
7   2.2E-2
6   1.3E-2
5   3.4E-3
4   -5.7E-3
3   -1.5E-2
2   -2.4E-2
1   -3.3E-2
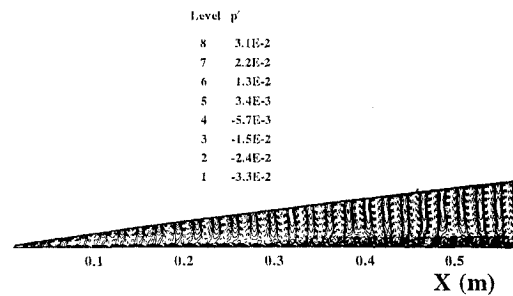
Figure 47: Instantaneous contours of pressure pertur-bations due to freestream acoustic wave for perfect gas at $M_\infty = 10$, $F = 0.5 \times 10^{-4}$ and $\theta_{ac} = 0°$.

Figure 45: Amplitude of pressure perturbations on the wall due to blowing and suction at $M_\infty = 10$, $F = 0.5 \times 10^{-4}$.

Level p'
8   4.6E-2
7   3.2E-2
6   1.9E-2
5   5.2E-3
4   -8.4E-3
3   -2.2E-2
2   -3.5E-2
1   -4.9E-2
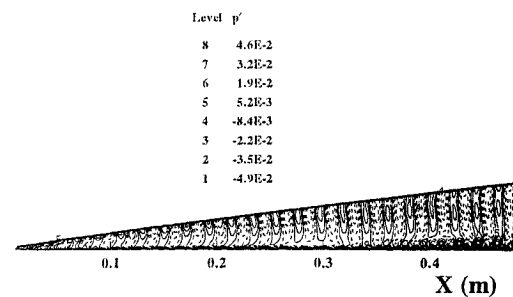
Figure 48: Instantaneous contours of pressure pertur-bations due to freestream acoustic wave for nonequilib-rium flow at $M_\infty = 10$, $F = 0.5 \times 10^{-4}$ and $\theta_{ac} = 0°$.
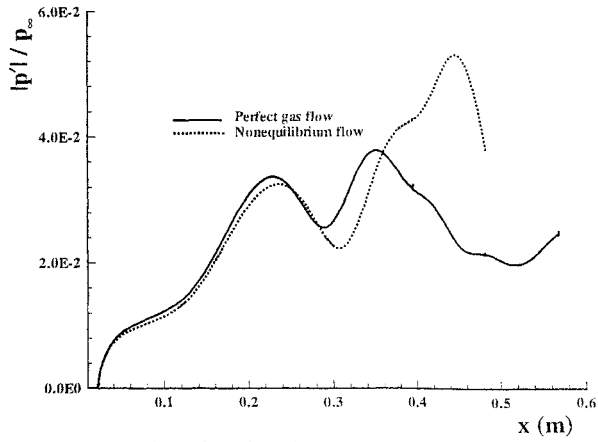
Figure 49: Amplitude of pressure perturbations on the wall due to freestream acoustic wave at $M_\infty = 10$, $F = 0.5 \times 10^{-4}$ and $\theta_{ac} = 0°$.
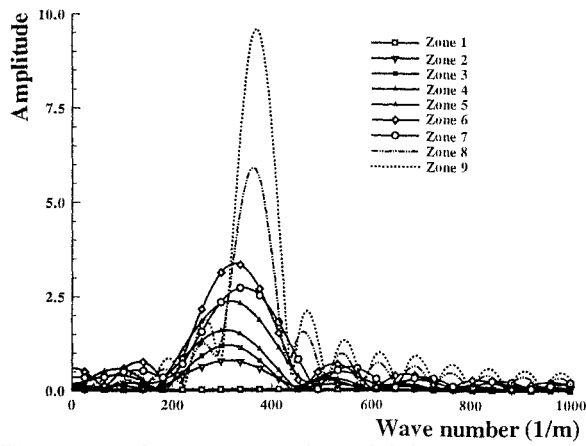
Figure 50: Components of spatial frequency for pressure perturbation on the wall ($M_\infty = 10$, $F = 0.5 \times 10^{-4}$).